Investigation of the 3D Printability of Covalently Cross-Linked Polypeptide-Based Hydrogels

Johnel Giliomee, Lisa C. du Toit, Bert Klumperman, and Yahya E. Choonara*
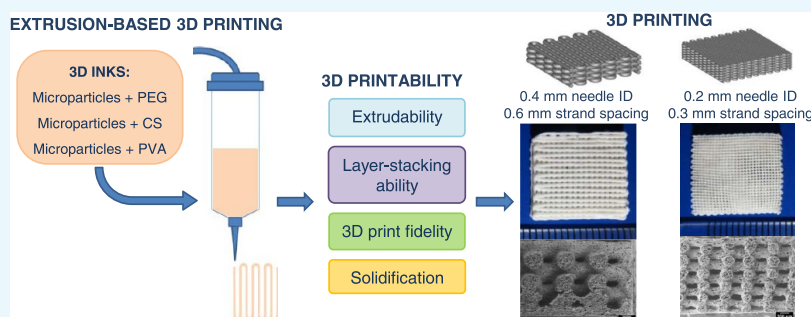
Read Online

ACCESS | Metrics & More | Article Recommendations | SI Supporting Information

ABSTRACT: The 3D printability of poly(L-lysine-*ran*-L-alanine) and four-arm poly(ethylene glycol) (P(KA)/4-PEG) hydrogels as 3D biomaterial inks was investigated using two approaches to develop P(KA)/4-PEG into 3D biomaterial inks. Only the "composite microgel" inks were 3D printable. In this approach, P(KA)/4-PEG hydrogels were processed into microparticles and incorporated into a polymer solution to produce a composite microgel paste. Polymer solutions composed of either 4-arm PEG-acrylate (4-PEG-Ac), chitosan (CS), or poly(vinyl alcohol) (PVA) were used as the matrix material for the composite paste. The three respective composite microgel inks displayed good 3D printability in terms of extrudability, layer-stacking ability, solidification mechanism, and 3D print fidelity. The biocompatibility of P(KA)/4-PEG hydrogels was retained in the 3D printed scaffolds, and the biofunctionality of bioinert 4-PEG and PVA hydrogels was enhanced. CS-P(KA)/4-PEG inks demonstrated excellent 3D printability and proved highly successful in printing scaffolds with a narrow strand diameter (∼200 μm) and narrow strand spacing (∼500 μm) while the integrity of the vertical and horizontal pores was maintained. Using different needle IDs and strand spacing, certain physical properties of the hydrogels could be tuned, while the 3D printed porosity was kept constant. This included the surface area to volume ratio, the macropore sizes, and the mechanical properties. The scaffolds demonstrated adequate adhesion and spreading of NIH 3T3 fibroblasts seeded on the scaffold surfaces for 4 days. Consequently, the scaffolds were considered suitable for potential applications in wound healing, as well as other soft tissue engineering applications. Apart from the contribution to new 3D biomaterial inks, this work also presented a new and facile method of processing covalently cross-linked hydrogels into 3D printed scaffolds. This could potentially "unlock" the 3D printability of biofunctional hydrogels, which are generally excluded from 3D printing applications.

1. INTRODUCTION

Three-dimensional (3D) printing in the field of biomedical engineering has seen a rapid increase in popularity in the last few years. This includes applications in tissue engineering, regenerative medicine, therapeutic delivery systems, medical device fabrication, and disease modeling and diagnostics.[1−3] Using 3D printing to fabricate precisely designed 3D architectures according to computer-aided design (CAD) allows the fabrication of scaffolds with controlled properties such as porosity, permeability, and mechanical strength.[4−6] Controlling these properties are particularly important in tissue engineering, as it controls the ability to incorporate cells into the scaffolds through bioprinting or postprint cell seeding.[7,8] Hydrogels form a popular class of 3D printable biomaterials or biomaterial inks as they have recently been termed.[9,10] This is

mainly due to their tissue-mimicking properties, making them suitable for tissue engineering applications. A number of hydrogels are also suitable for bioprinting due to their mild processing conditions.[11,12]

Hydrogels are typically 3D printed as their precursor materials. Their gelation, during or after the 3D printing process, is then used as the solidification mechanism to produce the final hydrogel structure. To obtain ideal 3D

printed structures, the hydrogel precursor materials require adequate viscosity to maintain their structural integrity prior to cross-linking.[13] Strategies to increase the viscosity of the hydrogel precursor material include using increased polymer concentrations,[14] adding composite materials,[15−17] and using near gel-phase or gel-phase inks.[18−21] Near gel-phase inks include gelatin solutions that are 3D printed at temperatures near their sol−gel transition.[21] Gel-phase inks include partially cross-linked gels such as alginate solutions mixed with low concentrations of calcium chloride.[20] Rutz et al.[18] also reported the 3D printing of covalently cross-linked gel-phase inks. Through carefully controlled cross-linking, they demonstrated how partially cross-linked hydrogels can be 3D printed. Another example of gel-phase inks includes the jammed microgel ink recently reported by Highley et al.[22] While the hydrogel microparticles are in their gel phase, the jammed microgel displayed elastic behavior at low strains and shear thinning at high strain rates. For the solidification mechanisms, ionic cross-linking and chemical cross-linking through photopolymerization largely dominate the research on 3D printable hydrogels.[23] This is because the onset of the cross-linking can be controlled. Cross-linking through a spontaneous chemical reaction rather than through a response to a stimulus is typically time-dependent and more difficult to control. Hence, a large number of covalently cross-linked hydrogels with promising applications in tissue engineering have been excluded from 3D printing.

The poly(Lys$_{60}$-ran-Ala$_{40}$)/4-arm PEG (P(KA)/4-PEG) hydrogel explored in this study is an excellent example of a covalently cross-linked hydrogel, considered non-3D printable in conventional 3D printing terms. This hydrogel was previously reported as having good biocompatibility and antibacterial properties.[24] In a recent study by Giliomee et al.,[25] the compositional effects of P(KA)/4-PEG were further evaluated for potential applications in wound healing. In this investigation, two approaches to developing P(KA)/4-PEG into 3D printable biomaterial inks were investigated. The first approach was based on the partial cross-linking of hydrogels to produce pliable materials, as reported by Rutz et al.[18] By incorporating primary and secondary cross-linking mechanisms into the hydrogel precursor components, the biomaterial ink can be synthesized via the primary cross-linking, while the secondary cross-linking is responsible for postprint solidification. The second approach employed hydrogel microparticles incorporated into a composite microgel paste. Composite pastes incorporating inorganic particles or polymer particles in a hydrogel precursor solution have been reported as biomaterial inks for 3D printing.[16,26−28] Apart from the viscosity gain, the addition of such particles also adds biofunctionality to the material. The solidification of these composite inks is dependent on the gelation of the hydrogel in which the particles are suspended. To our knowledge, this is one of the first studies investigating composite microgel pastes as biomaterial inks for 3D printing.

The 3D printability of the P(KA)/4-PEG inks developed through these two approaches was assessed in terms of extrudability, layer-stacking ability, 3D print fidelity, and solidification.[13,29] The combination of these criteria is considered as the fundamental requirement for any extrusion-based 3D ink.[13,29] In addition, the properties of the composite microgel materials and the effect of the 3D printing pattern on the physical properties were evaluated. This was done by preparing "nonporous" 3D printed scaffolds to evaluate the inherent material properties and "porous" 3D printed scaffolds to evaluate the structure-dependent scaffold properties. It was proposed that the processing of P(KA)/4-PEG into 3D printed scaffolds will allow further tunability of the physical properties of P(KA)/4-PEG hydrogels while enhancing the biofunctionality of the scaffolds.

2. RESULTS AND DISCUSSION

2.1. Preparation of Biomaterial Inks. *2.1.1. "Partially Cross-Linked" Inks.* The cross-linking between P(KA) and 4-PEG-SG was well-studied in Giliomee et al.,[25] and the phase plot was employed to identify soft pliable gels. For the partially cross-linked inks, the soft gel with a concentration of 2 wt % and a 4:1 molar ratio was selected for further investigation. The reaction between the free amines from P(KA) and the N-hydroxysuccinimidyl ester from 4-PEG-SG can be seen as the primary cross-linking. The secondary cross-linking mechanism was introduced on the P(KA) through chemical conjugation with aryl azides. Aryl azides are known for their rapid photocross-linking without the need for photoinitiators.[30] The reaction involves the photolysis of aryl azides into reactive nitrene.[30] The cross-linking with amines through nitrene chemistry then takes place. Photoreactive chitosan with 4-azidobenzamide functionality has been produced by reacting the amines in chitosan with 4-azidobenzoic acid through EDC coupling.[31] The amines in P(KA) were similarly reacted with 4-azidobenzoic acid to produce P(KA)-Az. The characteristic azide peak at ∼2120 cm^{-1} confirmed the conjugation using FTIR (Figure 1). The decrease in amines due to conjugation
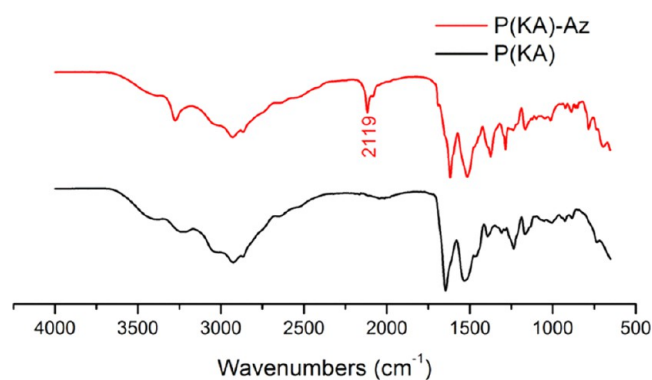

Figure 1. FTIR spectra of P(KA) before (black) and after (red) conjugation with 4-azidobenzoic acid.

was measured using the Kaiser assay. The degree of conjugation was then calculated using the difference in absorbance as a percentage of the initial absorbance of P(KA). The experimental degree of conjugation for the two targeted degrees of 20 and 40% was calculated as 32 and 58%, respectively. Since the primary cross-linking, as well as the secondary cross-linking, required free amines on P(KA), only partial conjugation of P(KA) was targeted. P(KA)-Az was then cross-linked with 4-PEG to form the ink, P(KA)-Az/4-PEG.

2.1.2. "Composite Microgel" Inks. Fine pastes of the P(KA)/4-PEG microparticles were prepared by adding 4-PEG-Ac, CS, or PVA polymer solutions to form the three respective composite microgel inks. FITC-stained microparticles were analyzed in dilute solutions as well as in the concentrated paste form using fluorescence microscopy. In the dilute solution, a combination of single and aggregated
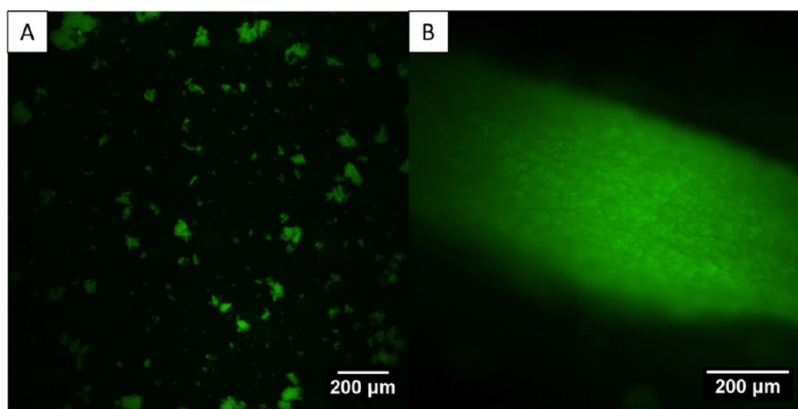
Figure 2. Fluorescence micrograph of microparticles of P(KA)/4-PEG labeled with FITC in (A) a dilute solution and (B) a concentrated paste.
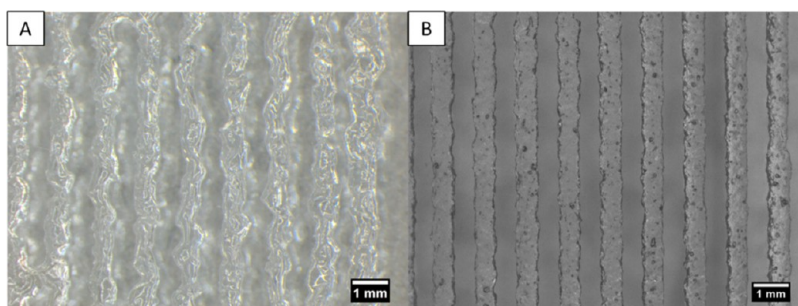

Figure 3. Images of the extruded strands of (A) P(KA)-Az/4-(PEG) and (B) CS-P(KA)/4-PEG (Authors' original image).

particles can be seen in Figure 2A. The morphology of the particles was irregular, with a broad size distribution. The mean diameter of the particles that were measurable (>10 μm) was 31.1 $\pm$ 19.8 μm. Nonetheless, the preparation method was preferred due to its robust application in producing fine pastes that pass through needle tips with 0.4 and 0.2 mm ID. In the concentrated paste, the particles are seen as closely packed together (Figure 2B).

2.2. Evaluation of the 3D Printability of the Biomaterial Inks. *2.2.1. Extrudability and Viscoelasticity.* The first criterion used for determining the 3D printability of prepared inks is their extrudability through the needle tip. The material needs to be extruded through the needle tip at a reasonable rate within the operating parameters of the 3D printer.[29] A reasonable rate will be fast enough to ensure a viable production time, while premature drying of extruded ink is prevented and slow enough to ensure optimal 3D print fidelity.[29] Furthermore, the morphology of the extruded material should be smooth and strand-like.[32] The morphology of the extruded partially cross-linked inks was seen as irregular discontinuous lumps of material (Figure 3A). The composite microgel inks, on the other hand, were extruded as smooth continuous strands (Figure 3B).

Ouyang et al.[32] demonstrated how the over-gelation of bioinks containing gelatin and alginate led to the extrusion of irregular and fragmented strand morphologies. Rutz et al.[18] further reported soft partially cross-linked gels with storage moduli (G') of 1−100 Pa as 3D printable, while stiff gels with G' higher than 150 Pa were not 3D printable. The gelation of P(KA)-Az/4-PEG with 32 and 58% conjugated Az equilibrated after ∼ 50 min at a G' of ∼220 Pa and ∼200 Pa, respectively (Figure 4). The G' of these partially cross-linked inks fall within the stiff non-3D printable range reported by Rutz et
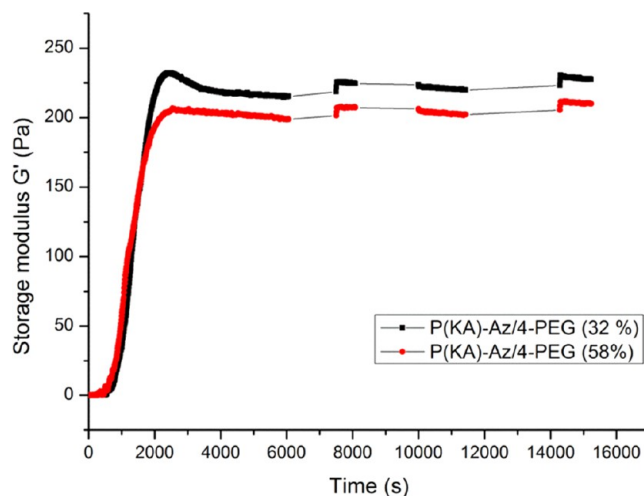

Figure 4. Development of storage modulus of P(KA)-Az/4-PEG with varying degrees of conjugation, indicating the primary cross-linking between 0 and 6000 s, and the secondary cross-linking from UV irradiation at ∼7500 and ∼15 000 s.

al.[18] However, preliminary studies on hydrogels with lower cross-linking degrees also led to the extrusion of fragmented, albeit softer gels. While Rutz et al. briefly reported certain gels as behaving similarly, no further explanation was provided.[18]

As part of the rheological characterization of the P(KA)-Az/4-PEG ink, a preliminary investigation into the secondary cross-linking was performed (Figure 4). After the inks were equilibrated for 6000 s, the rheological measurements were paused for 3 cycles. During the first cycle, the samples were UV irradiated for 10 min. This was followed by a control cycle without UV irradiation, while in the final cycle, the samples
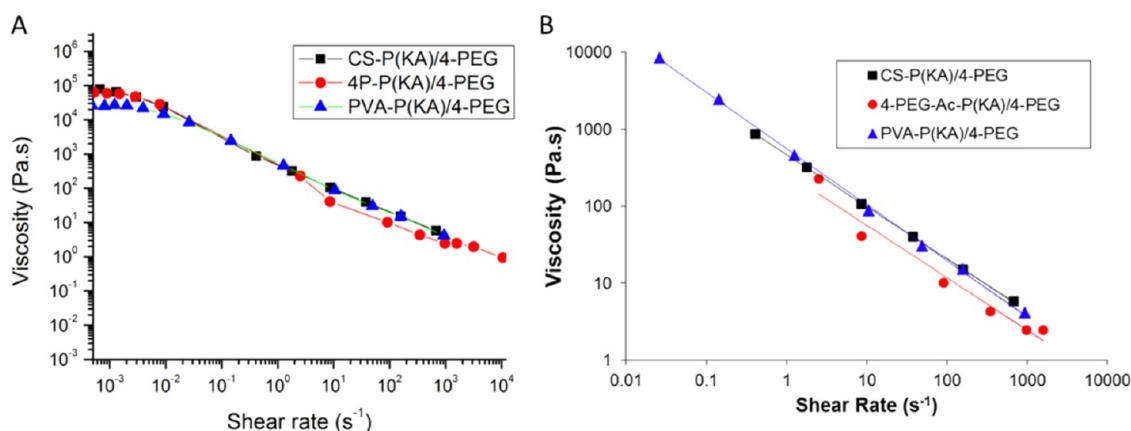
Figure 5. Viscosity behavior of the composite microgel inks showing shear thinning as the shear rate is increased (A) and the shear-thinning region fit to the power-law regression (B).

were UV irradiated for 20 min. However, the increase in G' after the two UV irradiation cycles was too small to have an effect on the solidification of the P(KA)-Az/4-PEG inks.

The composite microgel inks were expected to behave more like the jammed microgel inks, as reported by Highley et al.[22] At low strain, jammed microgels demonstrated an elastic response, while at increasing strain, the microgels reached a yielding point, followed by a shear-thinning response. The viscosity behavior of all of the composite microgel inks showed Newtonian behavior at low shear rates and non-Newtonian shear thinning between shear rates of 0.1 and 1000 s^{-1} (Figure 5). The shear-thinning regions of the plots were fitted to a power-law regression using the following equation

$$\eta = K\dot{\gamma}^{n-1} \tag{1}$$

where η is the viscosity (Pa·s), $\dot{\gamma}$ is the shear rate (s^{-1}), and K and n are shear-thinning coefficients as summarized in Table 1.

Table 1. Shear-Thinning Viscosity Coefficients, K and n of the Composite Microgel Inks

composite microgel ink	K	n
4-PEG-Ac-P(KA)/4-PEG	301	0.276
CS-P(KA)/4-PEG	471	0.321
PVA-P(KA)/4-PEG	563	0.270

Paxton et al.[29] used the viscosity coefficients to determine the average extrusion velocity, $\bar{\nu}$ of various materials using the following equation:

$$\bar{\nu} = \left(\frac{-\Delta P}{2LK}\right)\left(\frac{n}{3n+1}\right)R^{n+1/n} \tag{2}$$

where ΔP is the pressure, L is the needle length, and R is the needle diameter.[29] The calculated extrusion velocity at various printing parameters was then used to screen the materials according to a "3D printability window". They further found that materials with a larger 3D printability window in this screening method showed better 3D printability.[29] From four 3D printable materials identified by Paxton et al.,[29] K and n shear-thinning parameters ranged from 13.3 to 406 and 0.127 to 0.608, respectively.[29] Furthermore, one material with larger K and smaller n in comparison to the other materials showed a smaller 3D printability window.[29] The K coefficients of the composite microgel inks, summarized in Table 4, fall within or outside the upper range of the K coefficients from the 3D printable materials identified by Paxton et al. The n coefficients of the composite microgel inks, on the other hand, fall within the middle range. These combinations of K and n coefficients were not comparable to any of the 3D printable and non-3D printable materials tested by Paxton et al. It should be noted that the above calculation for $\bar{\nu}$ models the extrusion velocity based on a cylindrical needle, while a tapered needle was used
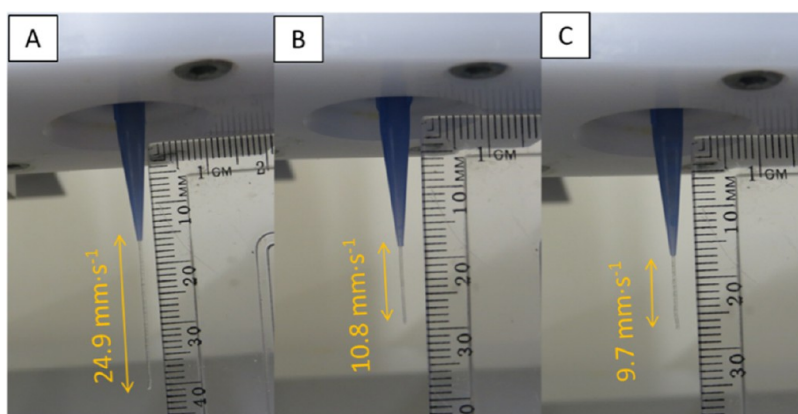

Figure 6. Images of the extruded strands of (A) 4-PEG-Ac-P(KA)/4-PEG at 0.5 bar, (B) CS-P(KA)/4-PEG at 1.5 bar, and (C) PVA-P(KA)/4-PEG at 1.1 bar after 1 s, indicating the extrusion velocities (yellow) calculated from the length of the strands (Authors' original image).
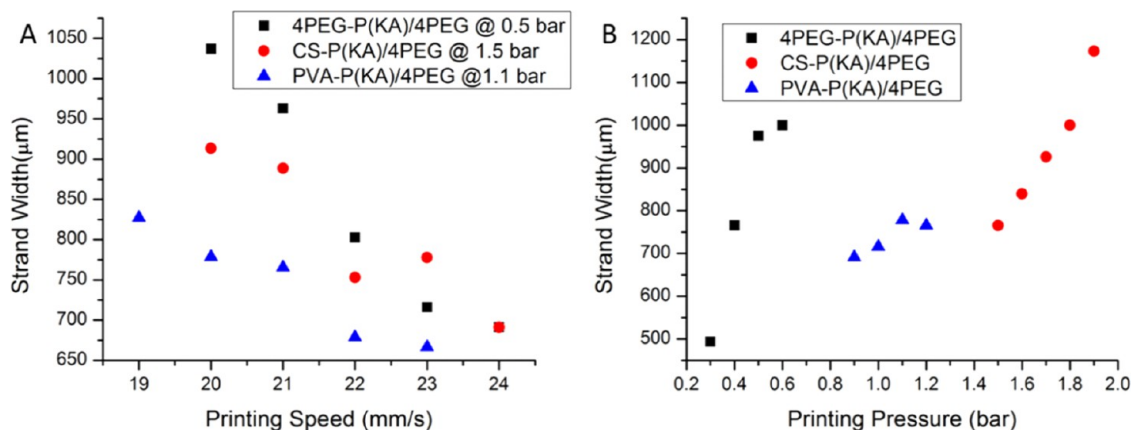
Figure 7. Effect of the 3D printing parameters on the strand width was investigated by varying the printing speed at constant pressures for the respective biomaterial inks (A) and varying the printing pressure at a constant speed of 20 mm/s (B).
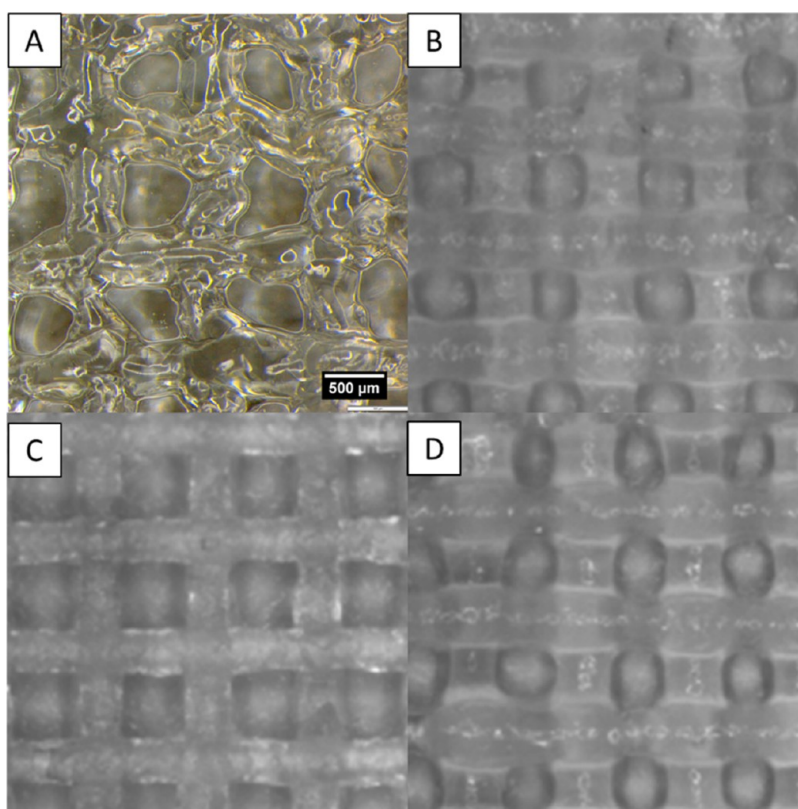

Figure 8. Images of the second 3D printed layers of the partially cross-linked P(KA)-Az/4-PEG ink (A) and the fourth 3D printed layers of the composite microgel inks, PEG-P(KA)/4-PEG (B), CS-P(KA)/4-PEG (C), and PVA-P(KA)/4-PEG (D), 3D printed with 0.4 mm needle ID and 1 mm strand spacing (B, C, and D were captured using the built-in camera from the 3D Bioplotter with the exact scale unknown) (Authors' original image).

in this study. Complex modeling of the flow dynamics inside tapered needles was beyond the scope of this study. Instead, we used the experimental extrusion velocity determined at specific extrusion pressures to evaluate the 3D printability of the composite microgel inks (Figure 6). The inks could be extruded through needle IDs of 0.4 and 0.2 mm at pressures within the instrumental limits (0.1−5.0 bar) of the 3D Bioplotter. Furthermore, the extrusion velocities were within the 3D printability window of 0−40 mm·s^{-1} as identified by Paxton et al.[29] Based on our experience with the 3D Bioplotter, this range can be justified for its good shape printing fidelity. The 4-PEG-Ac-P(KA)/4-PEG ink required the least pressure

and still extruded at a velocity of more than double the velocity of the other two inks. This correlates with the lower shear viscosities of 4-PEG-Ac-(PKA)/4-PEG measured at shear rates higher than ~2 s^{-1} (Figure 5). While 4-PEG-Ac-P(KA)/4-PEG had a similar n coefficient to PVA-P(KA)/4-PEG, PVA-P(KA)/4-PEG had a higher K coefficient, which could explain why it extruded at a lower velocity at a higher pressure. CS-P(KA)/4-PEG required a higher pressure to extrude at a velocity similar to PVA-P(KA)/4-PEG. This correlates with the trend in shear viscosities measured at shear rates higher than ~38 s^{-1}, where CS-P(KA)/4-PEG has a shear viscosity higher than PVA-P(KA)/4-PEG. This further correlates with
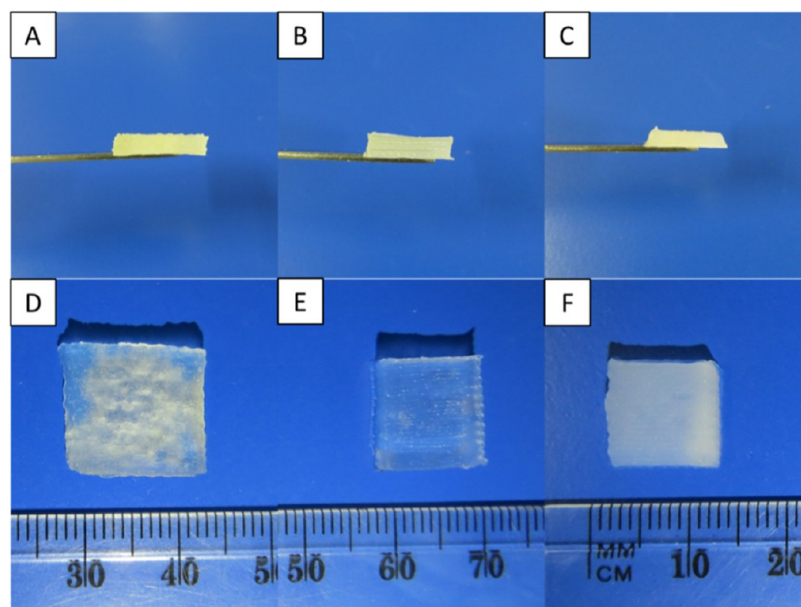
Figure 9. Photographic images of the nonporous 3D printed scaffolds, 4-PEG-Ac-P(KA)/4-PEG (A, D), CS-P(KA)/4-PEG (B, E), and PVA-P(KA)/4-PEG (C, F) (Authors' original image).

the higher n coefficient from CS-P(KA)/4-PEG, which indicates a weaker shear-thinning behavior in comparison to 4-PEG-Ac-(PKA)/4-PEG and PVA-P(KA)/4-PEG.[29] It further highlights the complexity of correlating shear viscosity measurements with 3D printing conditions. Small differences in the viscosity behavior of materials can have significant effects on their extrusion velocity and their shear rates within the 3D printing needle.

2.2.2. Strand Optimization and 3D Layer Stacking. The extrusion of the inks in the air is generally considered a good starting point for determining the printing parameters. However, further optimization of the pressure and printing speed was required to obtain good 3D print fidelity. The effect of these parameters on the strand width is shown in Figure 7. As expected, an increase in pressure at constant speed led to a higher material volume being dispensed per printing area and therefore a thicker strand width, while higher printing speed at constant pressure led to a lower material volume being dispensed per printing area, seen as a thinner strand width. When the material volume was too low, it led to a discontinuous strand. Images of the parametric effects on the strands can be seen in the Supporting Information (Figure S1).

The layer slicing height was further taken into account when selecting the strand width. The layer slicing height is an arbitrary input parameter used in the slicing process to convert the 3D CAD design into 2D layers. It translates to the needle offset between two consecutive layers, to account for the height of the dispensed material. For this study, a slicing height of 80% of the needle ID was selected. At strand widths matching the needle ID, this slicing height will allow adequate overlap between the layers and thereby good adhesion between the layers. Printing at larger strand widths will cause more overlap between the layers and essentially cause fusion of the layers and a loss of 3D print fidelity. It is noted from Figure 7 that the majority of the strand widths are larger than the needle ID of 0.4 mm. From our 3D printing experience with the 3D Bioplotter, good adhesion to the built plate is achieved by printing the first layer at a height of 80% of the needle

diameter. However, this causes flattening of the strands, which corrects after the third layer of printing.

3D layer stacking of the partially cross-linked ink, P(KA)-Az/4-PEG, further confirmed the nonprintability of these inks. Apart from the irregular morphology of the strands, the layers also fused together (Figure 8A). 3D layer stacking of the composite microgel inks showed that all three inks could be 3D printed in layers. Images documenting the first four layers of the 3D printing process of the composite microgel inks can be seen in Figure S2 and the Supporting Information. Closer inspection of the morphology of the layers after four layers were 3D printed showed slight fusion of the layers of 4-PEG-Ac-P(KA)/4-PEG and PVA-P(KA)/4-PEG (Figure 8B,D). The vertical pores formed by these inks can be seen as more rounded due to the sagging of the strands and the fusion of the layers. The CS-P(KA)/4-PEG inks showed excellent layer stacking properties after four layers were 3D printed. The strands showed no evidence of sagging, and the vertical pores had square morphologies (Figure 8C). Subsequently, CS-P(KA)/4-PEG inks were selected for further optimization of the 3D printing parameters to produce square scaffolds with 15 mm width and 2 mm height and different printing patterns (Table 6 and Figure S3).

2.2.3. Postprint Solidification and 3D Print Fidelity. The final step in determining the 3D printability of the composite microgel inks was to evaluate their solidification mechanism and 3D print fidelity. Nonporous 3D printing patterns of the composite microgel inks were investigated for this purpose. The solidification of the composite microgel inks was dependent on the gelation of the polymer solutions, 4-PEG-Ac, CS, and PVA, acting as a matrix material for the P(KA)/4-PEG hydrogel microparticles. All three inks produced stiff scaffolds that were able to be lifted with a spatula after their respective solidification procedures (Figure 9), demonstrating the successful incorporation of the hydrogel microparticles into a hydrogel matrix. However, the ease of the cross-linking and the postprint processing time for each ink is discussed below. Furthermore, the 3D print fidelity of the final scaffolds was

quantified in terms of dimensional deviations from the CAD dimensions.

Photo-cross-linking is widely used in 3D printing due to its ease of use and bioprinting applications.[33,34] The gelation of 4-PEG-Ac was based on the photopolymerization of the acrylate moieties in the presence of a photoinitiator (Irgacure 2959). In this study, 4-PEG-Ac-P(KA)/4-PEG was photo-cross-linked for 10 min to achieve complete solidification of all layers. Shorter cross-linking times led to incomplete solidification of lower layers, while longer cross-linking times caused drying around the edge of the scaffolds. Postprint washing of 4-PEG-Ac-P(KA)/4-PEG scaffolds was further required to remove cytotoxic photoinitiators. The cross-linking time correlates well with the postprint photo-cross-linking time of 7.5 min reported for PEG-diacrylate (PEGDA) inks.[35] In situ photo-cross-linking of each layer can eliminate the need for postprint photo-cross-linking. Also, using photoinitiators with low cytotoxicity, such as LAP, can eliminate the need for postprint washing. 4-PEG-Ac-P(KA)/4-PEG scaffolds showed substantial swelling, which led to a $33.3 \pm 1.5\%$ deviation from the CAD dimensions.

CS hydrogel scaffolds for tissue engineering applications have been produced through a variety of covalent and ionic cross-linking reactions.[36] The gelation of CS through neutralization of the solution pH was also reported. Ang et al.[37] 3D printed CS-based inks into a cross-linking solution containing sodium hydroxide (NaOH) to obtain fast neutralization of the acetic acid solution used to dissolve CS. Bergonzi et al.[38] further investigated different neutralizing agents such as potassium hydroxide (KOH), sodium bicarbonate, and ammonia vapors for the gelation of 3D printed CS. In this study, CS-P(KA)/4-PEG scaffolds were produced by freeze-drying and subsequent washing with ethanol and distilled water to remove residual acetic acid. Unwashed scaffolds, on the other hand, dissolved within less than 2 h. This solidification method required no optimization of cross-linking solutions, which can be difficult and tedious. However, the washing steps can add to the postprint processing time. Nonetheless, this method proved highly successful in retaining the 3D printed structures. A $16.4 \pm 2.7\%$ deviation in the overall scaffold dimensions in relation to the CAD dimensions was ascertained.

PVA is widely used in 3D printing as a supporting structure or a sacrificial material.[39,40] However, it rarely forms part of the final 3D printed scaffold. Kim et al.[21] reported the 3D printing of gelatine/PVA blends for hard tissue engineering applications. A popular method of producing PVA hydrogel scaffolds is through freeze−thaw cycles. It is well known that a larger number of cycles will lead to a stiffer gel due to an increase in the crystallinity of the polymer chains with every freezing step.[41] PVA-P(KA)/4-PEG scaffolds were prepared with 3−6 freeze−thaw cycles. While 3 cycles were adequate to provide solidification, the higher number of cycles led to a more robust construct. This method of postprint processing is very simple; however, it takes the longest compared to the 4-PEG-Ac-P(KA)/4-PEG and CS-P(KA)/4-PEG scaffolds. Based on the overall scaffold dimensions, PVA-P(KA)/4-PEG scaffolds led to the smallest deviation from the CAD dimensions. However, from Figure 9, it is observed that the PVA-P(KA)/4-PEG scaffold was tapered toward the top. Due to the number of repeat freeze−thaw cycles, it is likely that the scaffold dried slightly during the thawing process. Nonetheless, this effect can

be minimized by maintaining the scaffold in a sealed environment during the thawing process.

In addition to the nonporous 3D printed scaffolds, the 3D print fidelity of the porous 3D printed scaffolds of CS-P(KA)/4-PEG was evaluated in terms of their printing patterns (Table 2). The porous 3D printed scaffolds are further referred to as

Table 2. Percentage Deviation of the Strand Diameter and Interstrand Spacing of Hydrated Scaffolds Compared to Intended Printing Pattern Parameters

	dimensions (μm)		deviation (%)	
scaffold	strand diameter	interstrand spacing	strand diameter	interstrand spacing
0.2 mm scaffold	241 ± 18.0	297 ± 37.0	20.7 ± 9.0	7.9 ± 6.0
0.4 mm scaffold	457 ± 17.0	542 ± 28.0	14.2 ± 3.8	10.0 ± 4.0

the 0.4 mm scaffolds (0.4 mm needle ID) and the 0.2 mm scaffolds (0.2 mm needle ID) according to the printing patterns, as summarized in Table 6. The intended vertical and horizontal channels as a result of the cross-hatch printing pattern can be seen from the top and side views of the scaffolds (Figure 10B−E). The deviations from the intended printing patterns correlate with the overall deviation of the nonporous 3D printed CS-P(KA)/4-PEG scaffolds as a result of the material swelling. It should be noted that the strand optimization also played a role in the deviation from the printing pattern. The strand optimization used in this study was a crude process of balancing the strand diameter with the layer height. This was especially difficult with the smaller strand diameters of the 0.2 mm scaffold, as the layer height was prone to becoming too thin, which caused inadequate adhesion of extruded strands onto existing layers. Therefore, larger strand diameters were used for the 0.2 mm scaffold to ensure that the layer height remains optimized for the total printing process.

2.3. Evaluation of the Physical Properties of the Composite Microgel Scaffolds with nonporous 3D Printing Patterns. Since these scaffolds were fabricated with nonporous 3D printed patterns, the physical properties related to the inherent material properties of the developed composite microgel scaffolds. The inherent porosity of the composite microgel scaffolds of 4-PEG-Ac-P(KA)/4-PEG, CS-P(KA)/4-PEG, and PVA-P(KA)/4-PEG was evaluated using SEM (Figure 11). All of these scaffolds displayed an interconnected porous network. As summarized in Table 3, the average pore sizes of the scaffolds are within the ideal range of 20−125 μm reported for the regeneration of adult mammalian skin.[42] Further assessment of the percentage inherent porosity of the scaffolds indicated that CS-P(KA)/4-PEG has the highest porosity at 82.6%, while PVA-P(KA)/4-PEG had the lowest porosity at 64.4%. It was seen that the scaffolds with larger pore sizes did not necessarily have a higher porosity. Instead, the scaffolds that appeared to have higher interconnectivity and thinner membrane structures surrounding the pores had a higher % porosity. For tissue engineering applications, higher pore interconnectivity provides better mass transfer of nutrients and cellular waste.[42]

As discussed in a study by Giliomee et al.,[25] the equilibrium swelling ratio (ESR) is closely related to the network structure of hydrogels. The ESR of the composite microgel scaffolds followed the same trend as the pore sizes. The larger pore sizes
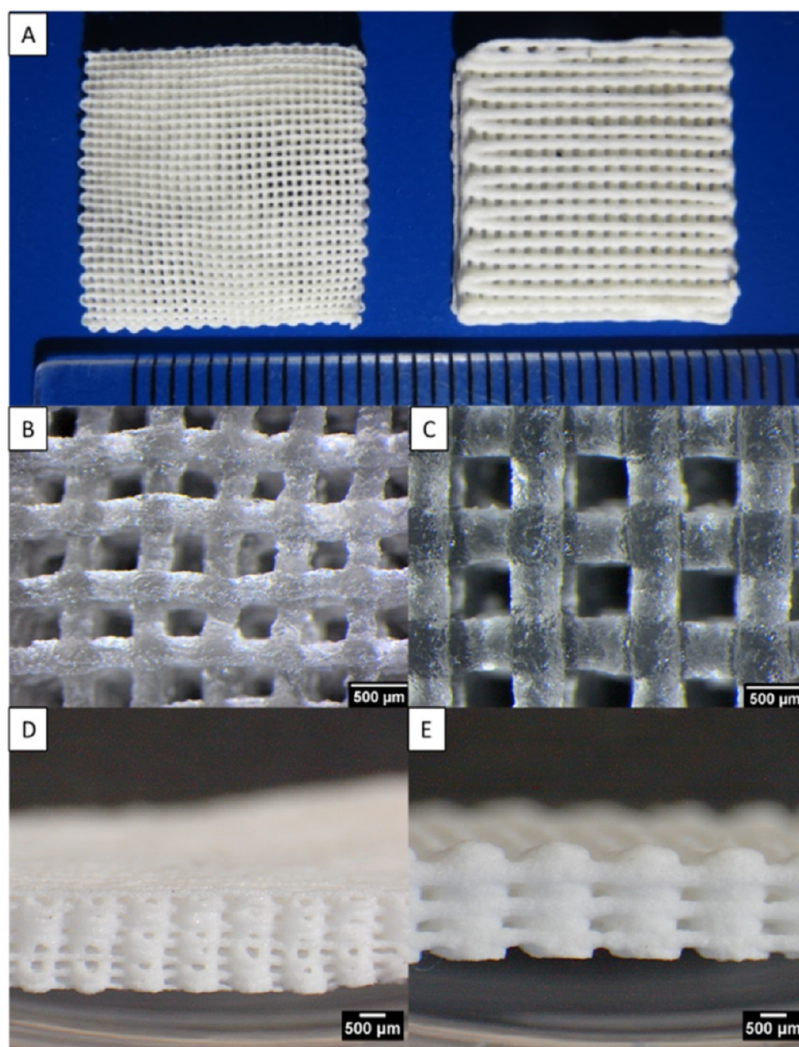
Figure 10. Images of the porous 3D printed CS-P(KA)/4-PEG 0.2 mm (A, LEFT) and 0.4 mm (A, RIGHT) scaffolds, and microscope images of the 0.2 mm (B, D) and 0.4 mm (C, E) scaffolds (top and side view). Scaffolds in A, D, and E were freeze-dried for better visualization. Scaffolds in B and C were hydrated (Authors' original image).
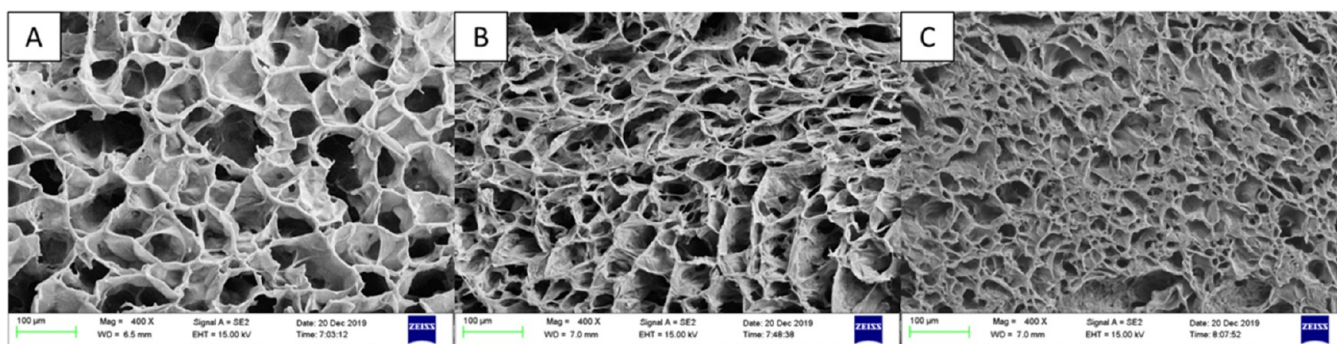

Figure 11. SEM micrographs of the cross-sections of freeze-dried composite hydrogels, 4-PEG-P(KA)/4-PEG (A), CS-P(KA)/4-PEG (B), and PVA-P(KA)/4-PEG (C), with the scale bars indicating 100 μm.

Table 3. Summary of the Physical Properties of the Composite Hydrogels, 4-PEG-P(KA)/4-PEG, CS-P(KA)/4-PEG, and PVA-P(KA)/4-PEG

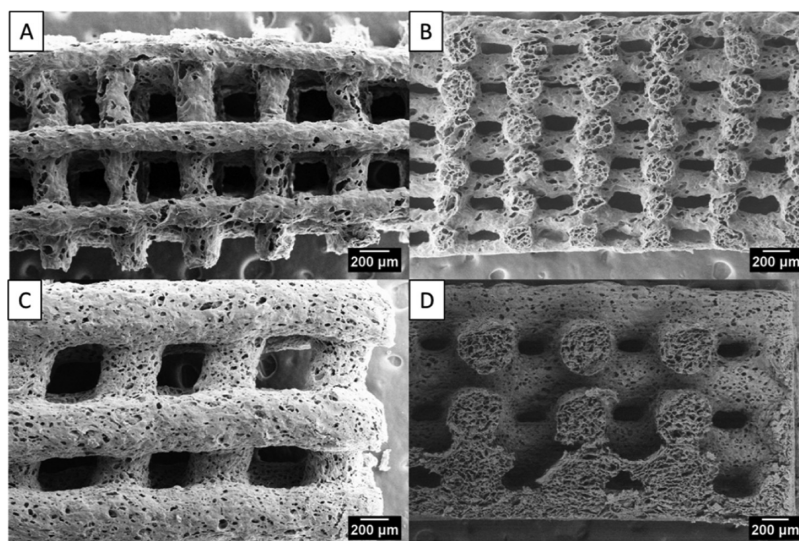| scaffold	average pore size (μm)	% porosity	equilibrium swelling ratio	tensile modulus (Pa)	compressive modulus (Pa)
4-PEG-Ac-P(KA)/4-PEG	102 ± 36	75.9	16.9 ± 2.0	203	235 ± 59
CS-P(KA)/4-PEG	72 ± 31	82.6	13.3 ± 0.8	132 ± 21	167 ± 41
PVA-P(KA)-4-PEG	33 ± 13	64.4	9.8 ± 1.0	711 ± 75	367 ± 3

Figure 12. SEM micrographs of the porous 3D printed scaffolds of CS-P(KA)/4-PEG, 0.2 mm scaffold (A, B), and 0.4 mm scaffold (C, D).

Table 4. Effect of 3D Printing on the Physical Properties of CS-P(KA)/4-PEG Scaffolds

scaffold (mm)	average pore size (μm)	porosity (%)	theoretical porosity (%)	A/V ratio	tensile modulus (Pa)	compressive modulus (Pa)
0.2	54 ± 20	98	40.3	16.8	91	45 ± 8
0.4	49 ± 18	98	39.6	8.8	82	147 ± 14

can indicate a more flexible network structure and, therefore, allow more swelling of the scaffold and vice versa.

Furthermore, the inherent mechanical properties of the 4-PEG-Ac-P(KA)/4-PEG, CS-P(KA)/4-PEG, and PVA-P(KA)/4-PEG scaffolds were assessed under tensile and compressive stress. PVA-P(KA)/4-PEG scaffolds had the highest moduli under tensile and compressive stress. It is further seen that CS-P(KA)/4-PEG had the lowest moduli. It has been shown that porosity can play an important role in the mechanical properties of hydrogels.[43] In this study, a higher porosity of the composite microgel scaffolds corresponded with lower mechanical properties. The materials reported here can be classified as microgel-filled hydrogels, as defined by Richtering and Saunders.[44] Since no chemical or physical cross-linking between the microparticles and the hydrogel matrix was employed, the composite systems were not expected to have an increased modulus compared to the parent hydrogels.[44]

2.4. Effect of the 3D Printing Pattern on the Physical Properties of CS-P(KA)/4-PEG Scaffolds. Micropores spread over the surface of the strands of the porous 3D printed scaffolds were visible with SEM (Figure 12). However, these were combined with nonporous areas, indicating the formation of surface skin due to the freeze-drying process. Cross-sections of the scaffolds showed interconnected porous networks within the strands. The average sizes of these micropores (Table 4) were slightly smaller than the pores from the nonporous 3D printed scaffolds of CS-P(KA)/4-PEG. The formation of micropores was driven by the formation of ice crystals during the freeze-drying process. It is known that the rate of freezing affects the size of the crystals. Due to the larger surface area to volume ratio of the porous 3D printed scaffolds compared to the nonporous scaffolds, they are expected to freeze faster than the nonporous 3D printed scaffolds and could explain the decrease in pore sizes as a result of 3D printing. The differences in the micropore sizes between the

0.2 mm scaffolds and the 0.4 mm scaffolds were found to be insignificant ($p > 0.05$).

The macroporosity resulting from the 3D printing pattern shows the formation of square vertical channels running into the face of the scaffolds (Figure 12A,C). These channels are intersected by horizontal channels running into the cross-section of the scaffolds, forming an interconnected network of channels (Figure 12B,D). The distance between the strands was determined in the hydrated form as 297 ± 37 and 542 ± 28 μm for the 0.2 and 0.4 mm scaffolds, respectively (Table 2). The theoretical macroporosities of the 3D printed scaffolds were further calculated from CAD models based on the experimental input parameters for the strand diameter and strand spacing. As expected, the 3D printed porosity of the 0.2 mm scaffolds was similar to the 0.4 mm scaffolds since the strand spacing, as well as the strand diameter, was changed with a factor of 2. On the other hand, the surface area to volume ratio (A:V ratio) of the 0.2 mm scaffold is almost 2 times larger than the 0.4 mm scaffold. The larger surface area is favorable to a higher cell infiltration.

The macroporosity from the 3D printing patterns was further seen to affect the mechanical properties of CS-P(KA)/4-PEG scaffolds. Under tensile stress, the porous 3D printed scaffolds had lower moduli than the nonporous 3D printed CS-P(KA)/4-PEG scaffolds. However, the difference between the 0.2 mm scaffolds and the 0.4 mm scaffold was very small. Under compressive stress, the 0.4 mm scaffolds had a slightly lower modulus compared to the nonporous 3D printed scaffold, while the modulus of the 0.2 mm scaffold was more than three times smaller (Table 4). Schipani et al.[45] correlated the change in the 3D printing pattern of PCL scaffolds with a change in scaffold porosity and used the latter to justify the differences in the compressive moduli of different scaffolds. For example, by increasing the strand spacing and thereby increasing the porosity, the compressive modulus was found to decrease. Furthermore, by decreasing the strand diameter,
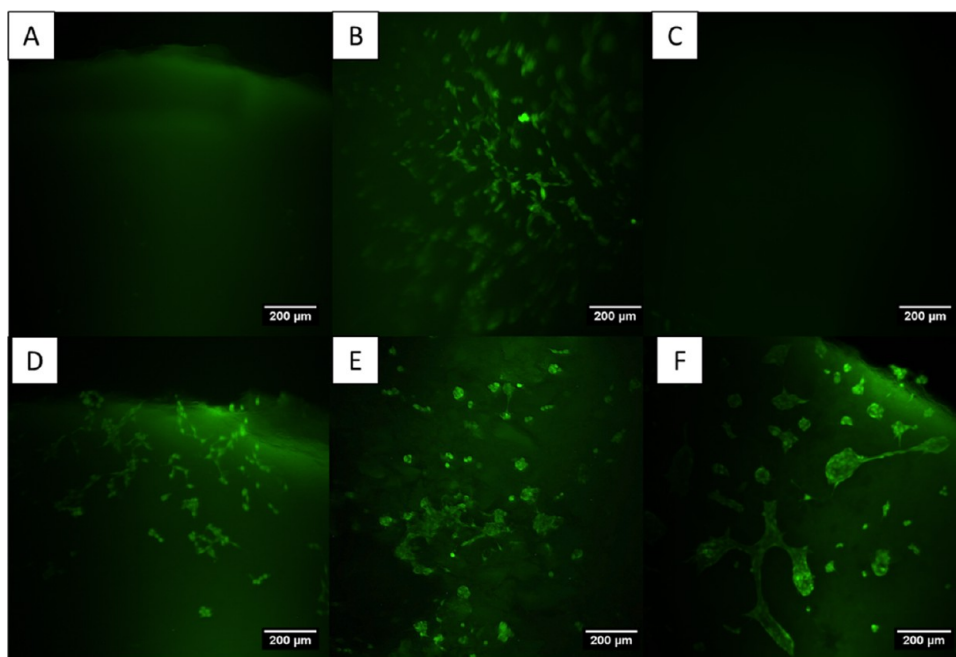
Figure 13. Micrographs of CFDA-SE-stained 3T3 fibroblasts cultured for 72 h on the 4-PEG-Ac hydrogel (A), CS hydrogel (B), PVA hydrogel (C), 4-PEG-Ac-P(KA)/4-PEG (D), CS-P(KA)/4-PEG (E), and PVA-P(KA)/4-PEG (F).
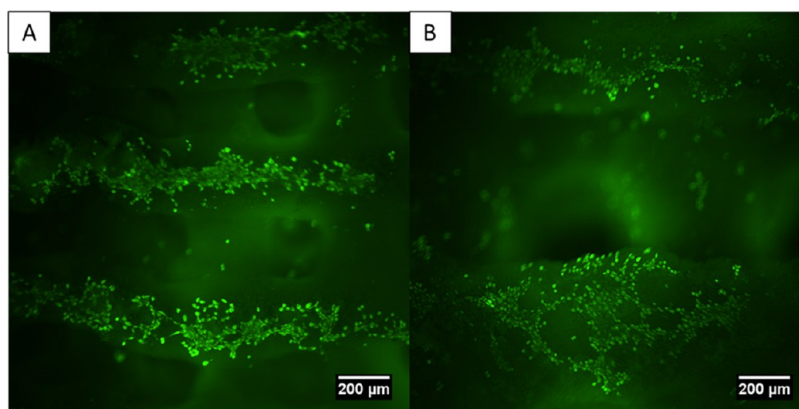

Figure 14. Micrographs of CFDA-SE-stained 3T3 fibroblasts cultured for 96 h on 0.2 mm scaffolds (A) and 0.4 mm scaffolds (B).

the porosity was increased and the compressive modulus decreased. However, they did not model the effect of strand diameter at constant porosity on the mechanical properties.

2.5. Effect of P(KA)/4-PEG Microparticles on the Biocompatibility of the Composite Microgels. The adhesion and migration of NIH 3T3 mouse fibroblasts on 4-PEG-Ac-P(KA)/4-PEG, CS-P(KA)/4-PEG, and PVA-P(KA)/4-PEG scaffolds were qualitatively assessed with fluorescence microscopy in comparison to 4-PEG-Ac, CS, and PVA hydrogels (Figure 13). On the 4-PEG-Ac and the PVA hydrogels, no attached cells were observed on the hydrogel surface. PEG is widely used for its hydrogel properties.[46] However, due to its hydrophilicity and low protein adsorptivity, PEG is also known for its low cell adhesion properties.[46] PVA is also known to have low cell adhesion properties. The CS hydrogels, on the other hand, showed that large numbers of cells spread over the hydrogel surface. This was in agreement with the well-known cell adhesion properties of CS hydrogels.[47] On the composite microgel scaffolds, clusters of cells are seen as spreading over the scaffold surfaces

(Figure 13D−F). Therefore, the addition of P(KA)/4-PEG microparticles to PEG and PVA greatly enhanced the biofunctionality of these hydrogels.

Furthermore, the spreading of 3T3 cells on the porous 3D printed CS-P(KA)/4-PEG scaffolds was also visualized (Figure 14). After 4 days of culturing, the cells were seen as migrating along the 3D printed strands. It has been reported that the behavior of adult human dermal fibroblast cells is largely influenced by the mechanical properties of scaffolds.[48,49] Nonetheless, this qualitative assessment indicated that the porous 3D printed scaffolds provided an adequate environment for adhesion and migration despite the differences in the mechanical properties between the porous and nonporous 3D printed scaffolds. This favorable behavior of NIH/3T3 fibroblast cells indicated that the scaffolds could be considered suitable for potential wound healing applications. Fibroblasts are known for their critical role in the wound healing process, including their synthesis of collagen.[50] Furthermore, NIH/3T3 fibroblast cells have been used in numerous studies evaluating the wound healing potential of scaffolds.[24,51,52] The demon-

strated biocompatibility, along with the low mechanical properties of the 3D printed scaffolds, also indicated that the scaffolds could be suitable for other soft tissue engineering applications, such as neural regeneration.

3. CONCLUSIONS

From the two approaches investigated to develop P(KA)/4-PEG hydrogels into biomaterial inks, only the composite microgel inks were 3D printable. These inks could be produced through the facile processing of P(KA)/4-PEG hydrogels into fine microparticles. The incorporation of these microparticles into polymer matrices afforded robust self-supporting inks, able to be 3D printed with high fidelity. Moreover, this approach demonstrated great versatility in terms of the hydrogel matrix components and the solidification mechanisms, with all three tested composite microgel inks showing good 3D printability. The physical properties of the 3D printed scaffolds could also be tuned based on the hydrogel matrix components. Based on the criteria used to assess the 3D printability, CS-P(KA)/4-PEG ink demonstrated the best properties. This ink proved highly successful in printing scaffolds with narrow strand diameter ($\sim$200 μm) and narrow strand spacing ($\sim$500 μm), while the integrity of the vertical and horizontal pores was maintained. Using different needle IDs and strand spacing, certain physical properties of the hydrogels could be tuned, while the porosity was kept constant. This included the surface area to volume ratio, the macropore sizes, and the mechanical properties. Furthermore, this approach of incorporating P(KA)/4-PEG microparticles into the composite microgel inks proved successful in retaining the biocompatibility of P(KA)/4-PEG hydrogels and enhanced the biofunctionality of the bioinert 4-PEG and PVA hydrogels. The limitations in applying these 3D biomaterial inks include their printing resolution. For extrusion-based 3D printing technology, minimum strand diameters of $\sim$100 μm are typically reported, while the presence of microparticles in the composite microgel inks will further limit the minimum printable strand diameters. This resolution is relatively low, compared to the $\sim$1 μm resolution that is achievable with laser-based technologies. Future investigations will focus on the structure-function relationship of the 3D printing pattern of the CS-P(KA)/4-PEG scaffolds in an *in vivo* environment such as a model wound site to determine potential benefits for wound healing. This study has also indicated the potential for incorporating other covalently cross-linked polypeptide-based hydrogels into 3D biomaterial inks and will prompt future investigations in the development of new 3D biomaterial inks with applications in different fields of biomedical engineering.

4. MATERIALS AND METHODS

All chemicals and solvents were purchased from commercial sources and used without further purification unless stated otherwise. Dry solvents were used as received and handled under dry inert gas. 4-Azidobenzoic acid (2 M in *tert*-butyl methyl ether), *N*-(3-dimethylaminopropyl)-*N*′-ethylcarbodii-mide hydrochloride (EDC), *N*,*N*,*N*′,*N*′-tetramethylethylenedi-amine (TEMED), 2-hydroxy-4′-(2-hydroxyethoxy)-2-methyl-propiophenone (Irgacure 2959), fluorescein-5-isothiocyanate (FITC), 5-carboxyfluorescein diacetate succinimidyl ester (CFDA-SE), chitosan (medium molecular weight; 75−85% deacetylated), and poly(vinyl alcohol) (Mw = 89 000−98 000, 99% hydrolyzed) were purchased from Sigma-Aldrich (St.

Louise, MO). 4-Arm PEG succinimidyl glutarate (10 kDa) and 4-arm PEG-acrylate (10 kDa) were purchased from JenKem Technology. All camera and microscope images were processed using ImageJ (version 1.51n) software. Fourier transform infrared (FTIR) spectrometry was performed on a Spectrum 100 FTIR Spectrometer (PerkinElmer) fitted with a Universal ATR Sampling Accessory.

4.1. Synthetic Procedures. *4.1.1. Functionalization of poly(Lys$_{60}$-ran-Ala$_{40}$) with 4-Azidobenzoic Acid.* Degrees of conjugation of 20 and 40% were targeted. For the 20% conjugation, the following procedure was used.

Poly(Lys$_{60}$-*ran*-Ala$_{40}$) P(KA) (synthesized as described in Giliomee et al.[25]) (200 mg) was dissolved in 15 mL of distilled water. 4-Azidobenzoic acid solution (2 M, 1.0 mL, 0.24 mmol), EDC (70 mg, 0.45 mmol), and TEMED (150 μL) were added to the P(KA) solution. The pH was then adjusted to 4−6, and the flask was covered with foil. The reaction was left to stir for 72 h, after which it was dialyzed against distilled water for 5 days. P(KA)-Az was obtained via lyophilization.

4.2. Preparation and Characterization of Hydrogel-Inks. *4.2.1. Approach 1: Partially Cross-linked Hydrogels.* Soft/gel-like materials of P(KA)-Az/4-PEG (as identified from Giliomee et al.[25]) were prepared according to the procedure described for P(KA)/4-PEG hydrogels with a concentration of 2 wt % and a 4:1 molar ratio.[25] Briefly, solutions of P(KA) (0.87 wt %) and 4-PEG-SG (1.13 wt %) were prepared in phosphate buffers of pH 9 and 4, respectively. Equal volumes of each were then combined and allowed to gel for 1 h. For these inks, functionalized P(KA)-Az replaced the P(KA) employed in Giliomee et al.[25]

4.2.2. Approach 2: Composite Microgel Pastes. P(KA)/4-PEG hydrogels with a concentration of 8 wt % and a 1:1 molar ratio were prepared according to the procedure described in Giliomee et al.[25] Briefly, solutions of P(KA) (1.29 wt %) and 4-PEG-SG (6.71 wt %) were prepared in phosphate buffers of pH 9 and 4, respectively. Equal volumes of each were then combined. After the hydrogel was equilibrated for 1 h, it was ground in its wet state with a mortar and pestle into a fine paste of P(KA)/4-PEG microparticles.

Three respective hydrogel precursor solutions were prepared as follows. A 4-arm PEG-acrylate (4-PEG-Ac) solution of 15 wt % was prepared in distilled water containing 0.5 wt % Irgacure 2959 and was degassed for 10 min under N$_2$ gas. A chitosan (CS) solution of 2 wt % was prepared in an acetic acid solution of 2% (v/v). A poly(vinyl alcohol) (PVA) solution of 10 wt % in distilled water was prepared by autoclaving to dissolve the PVA.

The P(KA)/4-PEG hydrogel microparticles were subsequently mixed with the hydrogel precursor solution of either 4-PEG-Ac, CS, or PVA at a 50:50 weight ratio (Table 5). The final weight of the ink was then adjusted to the initial P(KA)/4-PEG weight.

4.2.3. Fluorescence Microscopy. Fluorescence microscopy was used to assess the morphology and particle size of the P(KA)/4-PEG microparticles. P(KA)/4-PEG microparticles (20 mg) were diluted in 1 mL of distilled water. FITC (100 μL, 250 μM) in ethanol was diluted in 10 mL of water. The FITC solution (100 μL) was added to the microparticles and allowed to react for 20 min with the free amines present in the hydrogels. The microparticle solution (20 μL) was then placed between a microscope slide and a coverslip and viewed on a Leica MZ10F fluorescence microscope using a GFP3 filter with excitation wavelengths of 450−490 nm and barrier filter

Table 5. Summary of the Preparation of the Three Composite Microgel Pastes

biomaterial ink	P(KA)/4-PEG microparticles (50 wt %)	hydrogel precursor solution (50 wt %)
4-PEG-Ac-P(KA)/4-PEG	P(KA)/4-PEG (8 wt %; 1:1 molar ratio)	4-PEG-Ac (15 wt %) and Irgacure 2959 (0.5 wt %) in dist. H_2O
CS-P(KA)/4-PEG		CS (2 wt %) in acetic acid 2% (v/v)
PVA-P(KA)/4-PEG		PVA (10 wt %) in dist. H_2O

wavelengths of 500−550 nm. A Leica DFC365FX camera and LAP (v4.5, Leica) software were used to capture images with pseudocolor modifications matching the emission wavelength of FITC at 518 nm. The images were analyzed using ImageJ Software (version 1.51n), and the average particle sizes were calculated using 60 measurements. A particle of less than 10 μm could not be measured due to the resolution of the images.

4.3. 3D Printability of the Biomaterial Inks. *4.3.1. Viscoelasticity and Viscosity.* The primary and secondary cross-linking of P(KA)-Az/4-PEG was monitored on the ElastoSens Bio[2] until G' reached equilibrium. This nondestructive rheological technique allowed the assessment of the 2-step cross-linking process. The instrument makes use of a sample holder with a flexible membrane bottom. The sample's response to vibrations is measured using a laser, and built-in algorithms are then used to convert the data into shear storage modulus, G', and shear loss modulus, G''.

For the primary cross-linking, a total volume of 3 mL of the P(KA)-Az and 4-PEG-SG precursor solutions was added to a calibrated sample holder and the two components were manually mixed. The measurements of G' and G'' were started as soon as the P(KA)-Az and 4-PEG-SG components were mixed.

For the secondary cross-linking, the instrument measurements were paused for three cycles, while the sample was irradiated with a UV light source (365 nm wavelength) placed over the sample holder without disturbing the sample. For the first cycle, the sample was irradiated for 10 min. For the second cycle, the sample was not irradiated as a control to ensure no artificial effect on G' was caused as a result of the pausing. For the final cycle, the sample was irradiated for 20 min. This increased irradiation time served as a second experimental cycle to evaluate if further cross-linking occurred. The measurement after each cycle commenced until G' reached equilibrium.

The rotational shear viscosity of the composite microgel inks was measured on a Thermo Scientific HAAKE MARS Rheometer, with a 35 mm cone plate with a 1° incline and a 0.52 mm gap distance fitted with a HAAKE Universal Temperature Controller. The cone plate geometry has been employed for particle-containing samples[53] as long the gap height is at least 10 times higher than particle size.[54] The biomaterial inks (0.2 mL), prepared as described above, were placed on the rheometer plate and the viscosity (η) was measured as a function of shear rate ($\dot{\gamma}$) ranging from 0.0001 to 2000 s^{-1}. This allowed investigation into the shear-thinning viscosity behavior of the composite microgel inks.

4.3.2. Extrudability. The extrudability of the biomaterial inks through nozzle tips with 0.4 and 0.2 mm inner diameters (IDs) was investigated using the 3D Bioplotter (EnvisionTEC GmbH, Germany).

For the partially cross-linked inks, the precursor P(KA)-Az and 4-PEG solutions were added to the 30 mL syringe barrels (Nordson EFD) fitted with a plunger and a plastic tapered nozzle (Nordson EFD). The syringe barrel was then inserted into the printing head and left for 60 min to equilibrate at 25 °C.

The composite microgel pastes were added to syringe barrels fitted with a plunger, and the tip was closed with a stopper. The syringe barrel was then centrifuged at 4000 rpm for 5 min to remove any air bubbles.

The biomaterial inks were then extruded for 1 s at set pressures, and the morphology of the strands was visually analyzed. The length (mm) of the extruded strands were analyzed from digital images using ImageJ Software (version 1.51n) to determine the extrusion velocity (mm·s^{-1}).

4.3.3. Strand Optimization. Optimization of the strands was performed using the "manual parameter tuning" function on Visual Machine (version 2.8.130r7, Envisiontec GmbH) software to extrude single strands of the biomaterial inks at varied speed or pressure intervals to optimize the strand width. The built-in camera was used to capture images of the strands, and the images were calibrated using a 1 mm interval ruler.

4.3.4. 3D Printing. CAD models of 3D box-shaped geometries were prepared and converted into 2D layers using BioplotterRP (version 3.0, Envisiontec GmbH) slicer software. The slicing file was transferred to the Visual Machine algorithm for the layer-by-layer fabrication using the 3D Bioplotter (EnvisionTEC GmbH, Germany). The built-in algorithms were used to produce cross-hatch printing patterns by varying the strand diameter, the strand spacing, and the layer slicing height, while the orientation between the layers was set at 90° (Table 6 and Figure 15).

Table 6. Summary of the 3D Printing Patterns

cross-hatch pattern parameters	3D printed pattern		
	nonporous	porous	
strand diameter (mm)[a]	0.40	0.40	0.20
strand spacing (mm)	0.40	1.0	0.50
interstrand spacing (mm)[b]	0	0.60	0.30
layer slicing height (mm)	0.32	0.32	0.16
layer orientation (deg)	90	90	90

[a]Strand diameter based on the needle ID. [b]Interstrand spacing is the distance between the two adjacent strands.

Biomaterial inks were prepared and loaded into the syringe barrel as described under "Extrudability". 3D constructs were 3D printed using the parameters summarized in the Supporting Information (Table S1).

4.3.5. Postprint Solidification. Due to the varying chemical compositions of the different biomaterial inks prepared in this study, each ink required a solidification mechanism specific to the components of the ink.

After printing, the 4-PEG-Ac-P(KA)/4-PEG constructs were placed in a UV box fitted with a 365 nm wavelength light source and irradiated for 10 min. The UV-cross-linked scaffolds were then frozen at −20 °C overnight and further cooled to −60 °C before lyophilizing.

The CS-P(KA)/4-PEG constructs were frozen at −20 °C immediately after printing. After overnight freezing, the scaffolds were further cooled to −60 °C before lyophilizing. The scaffolds were then washed in absolute ethanol (99.9%),
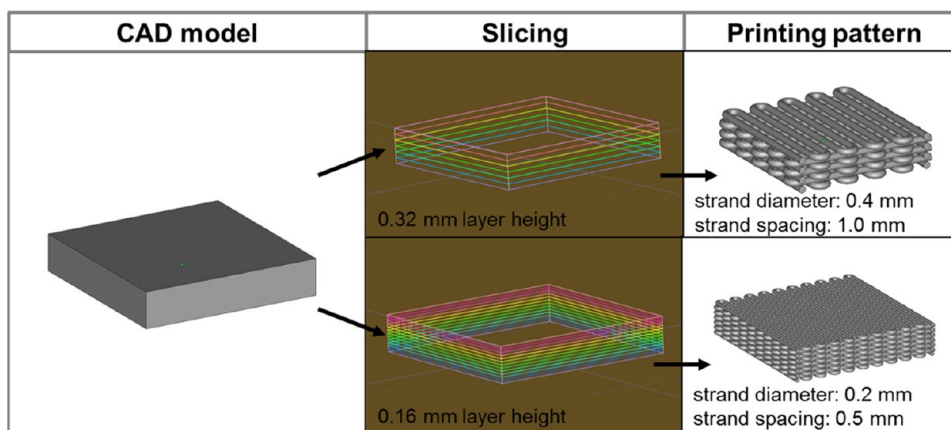
Figure 15. Schematic illustrates the slicing of the CAD model of the 3D box-shaped design with dimensions of $10 \times 10 \times 2$ mm^3 ($l \times w \times h$) into 2D layers using different layer heights of 0.32 and 0.16 mm, respectively, while the printing patterns are represented as 3D CAD models. The strand diameter was determined from the needle ID, while the strand spacing was selected through the built-in algorithms of Visual Machines (EnvisionTEC GmbH, Germany) used to fill-in the 2D layers.

followed by subsequent washes with ethanol in distilled water dilutions (90, 80, 70, 60, 50, 30, 10, and 0% ethanol). Each washing cycle was allowed to equilibrate for 1 h to remove any traces of acetic acid. The scaffolds were then lyophilized.

For the PVA-P(KA)/4-PEG constructs, the solidification was achieved by freeze−thaw cycles. Six cycles of freezing at −20 °C for 16 h followed by 8 h of thawing at room temperature were used to produce the physically cross-linked scaffolds. The scaffolds were then lyophilized.

4.3.6. 3D Print Fidelity. The dimensions of the 3D printed scaffolds in their hydrated state were compared to the intended dimensions, and the deviation was used as a measure of the 3D print fidelity. The scaffolds were solidified as per the *postprint solidification* method and then hydrated with distilled water before being measured. For the nonporous 3D printed scaffolds, three measurements per geometrical side (width, length, and height) were measured with a digital caliper. The % deviations from the intended CAD dimensions were calculated from the average measured dimensions. For the porous scaffolds, the strand diameter and interstrand spacing were measured using an Olympus SZX7 stereomicroscope. The average dimensions from three measurements were compared with the intended printing pattern in Table 6.

4.4. Scaffold Characterization. *4.4.1. Mechanical.* For the mechanical tests, all scaffold dimensions were determined from three measurements per geometrical side, measured with a digital caliper. The average of each side was then used to calculate the sample area. The respective moduli were calculated as the gradient of the linear section of stress vs strain plots. Stress and strain were calculated using the following equations

$$\text{stress} = \frac{F}{A} \tag{3}$$

$$\% \text{ strain} = \frac{\Delta d}{d_i} \times 100 \tag{4}$$

where F is the force applied in Newton (N), A is the calculated area over which the force is applied in mm^2, Δd is the change in sample dimension (in the direction of the force applied), and d_i is the initial sample dimension.

Compressive tests were performed on a TA.XT*plus* Texture Analyzer from Stable Micro Systems. 30% strain was applied to the samples hydrated in distilled H$_2$O at a rate of 1% s^{-1}.

Uniaxial tensile tests were performed using a BioTester (CellScale). The bio-rakes with a tine diameter of 305 μm and a tine spacing of 1.7 mm were used to mount the samples. The strain was increased from 0 to 30% over a duration of 60 s.

4.4.2. Swelling. The equilibrium swelling ratio (ESR) of the scaffolds was determined from the following equation

$$\text{ESR} = \frac{(W_W - W_D)}{W_D} \tag{5}$$

W_W is the wet weight of the hydrogel after swelling in PBS and W_D is the dry weight of the hydrogel after freeze-drying.

4.4.3. Porosity. The pore sizes were analyzed using scanning electron microscopy (SEM). Sections of the freeze-dried scaffolds were mounted on metal stubs using carbon tape and coated twice with carbon and once with gold/palladium using a sputter coater. Micrographs of the face and cross-sections were taken using a SIGMA 03-39 field emission electron microscope (FE SEM) (ZEISS). The images were analyzed using ImageJ Software (version 1.51n), and the average pore sizes were calculated using 40−60 measurements from 3 images with size distributions approximating normal distributions.
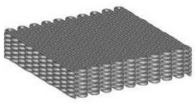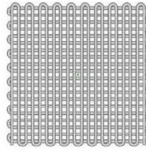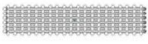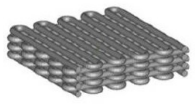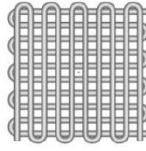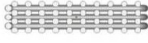
The porosity of the scaffolds was determined by determining the weight of the dry scaffold, W_1, and then placing it in ethanol, acting as an inert solvent. When there were no more visible air bubbles within the scaffold, the scaffold was removed and excess ethanol was removed from the surface with filter paper. The weight of the scaffold filled with ethanol was then taken as W_2. This was then used to calculate the volume of the pores, V_p, using the following equation

$$V_p = \frac{W_2 - W_1}{\rho_{\text{EtOH}}} \tag{6}$$

where ρ_{EtOH} is the density of ethanol at 25 °C (0.785 g·cm^{-3}). The porosity was then calculated as a percentage of the bulk scaffold volume, V_s, using the following equation

$$\% \text{ porosity} = \frac{V_p}{V_s} \times 100 \tag{7}$$

Table 7. Summary of the Model Input and Output Parameters and the Schematic Representations of the CAD Models

Model	3D View	Top View	Cross-section
Strand diameter: 0.241 mm Volume: 119 mm^3 Surface area: 2009 mm^2			
Strand diameter: 0.457 mm Volume: 120 mm^3 Surface area: 1062 mm^2			

The architectures of the porous 3D printed scaffolds were further modeled with CAD using SketchUp (version 15.3.331, Trimble). From the CAD model, the scaffold volume and surface area were determined using Magics (version 18.03, Materialize) (Table 7). The theoretical % porosity was calculated using the following equation

$$\% \text{ porosity} = \frac{V_s - V_m}{V_s} \times 100 \tag{8}$$

where V_s is the bulk scaffold volume and V_m is the modeled volume of the cross-hatch structure.

4.4.4. In Vitro Cell Adhesion Studies. NIH 3T3 mouse fibroblast cells were used for cell adhesion studies. The cells were cultured in a fresh medium composed of Dulbecco's Modified Eagle's Medium (DMEM) supplemented with 10% fetal bovine serum and 1% penicillin−streptomycin solution (10 000 units penicillin and 10 mg streptomycin/mL). For adhesion onto the nonporous scaffolds, small discs of the scaffolds were prepared by placing ∼30 μL of the biomaterial inks between a glass slide and coverslips with 1 mm spacers. The inks were then cross-linked using the solidification method described under "Solidification". The scaffolds were then sterilized under UV light (265 nm) for 10 min and hydrated in a fresh medium overnight. The scaffolds were then placed in 48 well plates, and 200 μL of cells in the fresh medium (15 000 cells/well) were added onto the scaffolds. The cells were then cultured for 72 h at 37 °C with 5% CO_2.

For adhesion onto the porous 3D printed scaffolds, 10 × 10 × 2 mm^3 scaffolds of CS-P(KA)/4-PEG were prepared as described above. The scaffolds were sterilized under UV light for 10 min and hydrated in the fresh medium overnight. The scaffolds were then placed in 12 well plates and 2 mL of cells in the fresh medium (75 000 cells/mL) were added onto the scaffolds. The cells were then cultured for 96 h at 37 °C with 5% CO_2.

To visualize the cells adhered to the scaffolds, the cells were stained with CFDA-SE. After the specified incubation times, the medium was carefully removed and replaced with equal volumes of 5 μM CFDA-SE in PBS (pH 7.2). The plates were then incubated for 8 min at 37 °C with 5% CO_2. The staining

solutions were then removed and replaced with equal volumes of fresh medium and incubated for 5 min. This washing step was repeated twice, and the scaffolds were then viewed on a Leica MZ10F fluorescence microscope using the same procedure described above for FITC stains.

4.5. Statistical Evaluation. Where appropriate, results were reported as mean ± standard deviation. One-way analysis of variance (ANOVA) and student's *t*-test were used for comparison between groups. A value of $p < 0.05$ was considered statistically significant.

◼ ASSOCIATED CONTENT

Ⓢ Supporting Information

The Supporting Information is available free of charge at https://pubs.acs.org/doi/10.1021/acsomega.1c05873.

Summary of the 3D printing parameters (Table S1); images of the printed strands of 4-PEG-Ac-P(KA)/4-PEG at different printing pressures and different printing speeds (Figure S1); images documenting the first four layers of the 3D printing process of the composite microgel inks 4-PEG-P(KA)/4-PEG, CS-P(KA)/4-PEG, and PVA-P(KA)/4-PEG 3D printed with 0.4 mm needle ID and 1 mm strand spacing (Figure S2); 3D printing of CS-P(KA)/4-PEG ink with 0.4 mm needle ID and 1.0 mm strand spacing and 0.2 mm needle ID and 0.5 mm strand spacing (Figure S3) (PDF)

◼ AUTHOR INFORMATION

Corresponding Author

Yahya E. Choonara − *Wits Advanced Drug Delivery Platform Research Unit, Department of Pharmacy and Pharmacology, School of Therapeutic Sciences, Faculty of Health Sciences, University of the Witwatersrand, Johannesburg 2193, South Africa;* ◉ orcid.org/0000-0002-3889-1529; Phone: +27-11-717-2052; Email: yahya.choonara@wits.ac.za; Fax: +27-86-553-4733

Authors

Johnel Giliomee − *Wits Advanced Drug Delivery Platform Research Unit, Department of Pharmacy and Pharmacology,*

School of Therapeutic Sciences, Faculty of Health Sciences, University of the Witwatersrand, Johannesburg 2193, South Africa

Lisa C. du Toit − Wits Advanced Drug Delivery Platform Research Unit, Department of Pharmacy and Pharmacology, School of Therapeutic Sciences, Faculty of Health Sciences, University of the Witwatersrand, Johannesburg 2193, South Africa

Bert Klumperman − Department of Chemistry and Polymer Science, Faculty of Science, Stellenbosch University, Stellenbosch 7600, South Africa; ⊙ orcid.org/0000-0003-1561-274X

Complete contact information is available at:
https://pubs.acs.org/10.1021/acsomega.1c05873

Author Contributions

This manuscript was written through contributions of all authors. All authors have given approval to the final version of the manuscript.

Notes

The authors declare no competing financial interest.

■ ACKNOWLEDGMENTS

The late Prof. Viness Pillay was the Director of the Wits Advanced Drug Delivery Platform Research Unit and integral to the initial project conceptualization. He passed away before the submission of this manuscript.

■ REFERENCES

(1) Ahangar, P.; Cooke, M. E.; Weber, M. H.; Rosenzweig, D. H. Current Biomedical Applications of 3D Printing and Additive Manufacturing. *Appl. Sci.* **2019**, *9*, No. 1713.

(2) Jamróz, W.; Szafraniec, J.; Kurek, M.; Jachowicz, R. 3D Printing in Pharmaceutical and Medical Applications − Recent Achievements and Challenges. *Pharm. Res.* **2018**, *35*, No. 176.

(3) Ngo, T. D.; Kashani, A.; Imbalzano, G.; Nguyen, K. T. Q.; Hui, D. Additive manufacturing (3D printing): A review of materials, methods, applications and challenges. *Compos. Part B: Eng.* **2018**, *143*, 172.

(4) Yang, S.; Leong, K.-F.; Du, Z.; Chua, C.-K. The Design of Scaffolds for Use in Tissue Engineering. Part II. Rapid Prototyping Techniques. *Tissue Eng.* **2002**, *8*, 1−11.

(5) Mota, C.; Puppi, D.; Chiellini, F.; Chiellini, E. Additive manufacturing techniques for the production of tissue engineering constructs. *J. Tissue Eng. Regen. Med.* **2015**, *9*, 174.

(6) Kelly, C. N.; Miller, A. T.; Hollister, S. J.; Guldberg, R. E.; Gall, K. Design and Structure−Function Characterization of 3D Printed Synthetic Porous Biomaterials for Tissue Engineering. *Adv. Healthc. Mater.* **2018**, *7*, No. 1701095.

(7) Fan, D.; Staufer, U.; Accardo, A. Engineered 3D Polymer and Hydrogel Microenvironments for Cell Culture Applications. *Bioengineering* **2019**, *6*, No. 113.

(8) Singh, M.; Jonnalagadda, S. Advances in bioprinting using additive manufacturing. *Eur. J. Pharm. Sci.* **2020**, *143*, No. 105167.

(9) Kirchmajer, D. M.; Gorkin, R., III; in het Panhuis, M. An overview of the suitability of hydrogel-forming polymers for extrusion-based 3D-printing. *J. Mater. Chem. B* **2015**, *3*, 4105.

(10) Groll, J.; Burdick, J. A.; Cho, D.-W.; Derby, B.; Gelinsky, M.; Heilshorn, S. C.; Jüngst, T.; Malda, J.; Mironov, V. A.; Nakayama, K.; Ovsianikov, A.; Sun, W.; Takeuchi, S.; Yoo, J. J.; Woodfield, F. A definition of bioinks and their distinction from biomaterial inks. *Biofabrication* **2019**, *11*, No. 013001.

(11) Gopinathan, J.; Noh, I. Recent trends in bioinks for 3D printing. *Biomater. Res.* **2018**, *22*, No. 11.

(12) Panwar, A.; Tan, L. P. Current Status of Bioinks for Micro-Extrusion-Based 3D Bioprinting. *Molecules* **2016**, *21*, No. 685.

(13) Kyle, S.; Jessop, Z. M.; Al-sabah, A.; Whitaker, I. S. " Printability" of Candidate Biomaterials for Extrusion Based 3D Printing: State-of-the-Art. *Adv. Healthcare Mater.* **2017**, *6*, No. 1700264.

(14) Schuurman, W.; Levett, P. A.; Pot, M. W.; van Weeren, P. R.; Dhert, W. J. A.; Hutmacher, D. W.; Melchels, F. P. W.; Klein, T. J.; Malda, J. Gelatin-Methacrylamide Hydrogels as Potential Biomaterials for Fabrication of Tissue-Engineered Cartilage Constructs. *Macromol. Biosci.* **2013**, *13*, 551.

(15) Narayanan, L. K.; Huebner, P.; Fisher, M. B.; Spang, T.; Starly, B.; Shirwaiker, R. A. 3D-Bioprinting of Polylactic Acid (PLA) Nanofiber−Alginate Hydrogel Bioink Containing Human Adipose-Derived Stem Cells. *ACS Biomater. Sci. Eng.* **2016**, *2*, 1732.

(16) Wang, X.; Tolba, E.; Schröder, H. C.; Neufurth, M.; Feng, Q.; Diehl-Seifert, B.; Müller, W. E. G. Effect of bioglass on growth and biomineralization of SaOS-2 cells in hydrogel after 3D cell bioprinting. *PLoS One* **2014**, *9*, No. e112497.

(17) Martínez-Vázquez, F. J.; Cabañas, M. V.; Paris, J. L.; Lozano, D.; Vallet-Regí, M. Fabrication of novel Si-doped hydroxyapatite/gelatine scaffolds by rapid prototyping for drug delivery and bone regeneration. *Acta Biomater.* **2015**, *15*, 200.

(18) Rutz, A. L.; Hyland, K. E.; Jakus, A. E.; Burghardt, W. R.; Shah, R. N. A Multimaterial Bioink Method for 3D Printing Tunable, Cell-Compatible Hydrogels. *Adv. Mater.* **2015**, *27*, 1607.

(19) Lewis, P. L.; Green, R. M.; Shah, R. N. 3D-printed gelatin scaffolds of differing pore geometry modulate hepatocyte function and gene expression. *Acta Biomater.* **2018**, *69*, 63.

(20) Lee, H.; Ahn, S.; Bonassar, L. J.; Kim, G. Cell(MC3T3-E1)-Printed Poly(ε-caprolactone)/Alginate Hybrid Scaffolds for Tissue Regeneration. *Macromol. Rapid Commun.* **2013**, *34*, 142.

(21) Kim, H.; Hoon, G.; Hyun, C.; Suk, Y.; Kim, G. Gelatin/PVA scaffolds fabricated using a 3D-printing process employed with a low-temperature plate for hard tissue regeneration: Fabrication and characterizations. *Int. J. Biol. Macromol.* **2018**, *120*, 119.

(22) Highley, C. B.; Song, K. H.; Daly, A. C.; Burdick, J. A. Jammed Microgel Inks for 3D Printing Applications. *Adv. Sci.* **2019**, *6*, No. 1801076.

(23) Song, A.; Rane, A. A.; Christman, K. L. Antibacterial and cell-adhesive polypeptide and poly(ethylene glycol) hydrogel as a potential scaffold for wound healing. *Acta Biomater.* **2012**, *8*, 41.

(24) Li, J.; Wu, C.; Chu, P. K.; Gelinsky, M. 3D printing of hydrogels: Rational design strategies and emerging biomedical applications. *Mater. Sci. Eng.: Rep.* **2020**, *140*, No. 100543.

(25) Giliomee, J.; du Toit, L. C.; Kumar, P.; Klumperman, B.; Choonara, Y. E. Evaluation of Composition Effects on the Physicochemical and Biological Properties of Polypeptide-Based Hydrogels for Potential Application in Wound Healing. *Polymers* **2021**, *13*, No. 1828.

(26) Wüst, S.; Godla, M. E.; Müller, R.; Hofmann, S. Tunable hydrogel composite with two-step processing in combination with innovative hardware upgrade for cell-based three-dimensional bioprinting. *Acta Biomater.* **2014**, *10*, 630.

(27) Haberstroh, K.; Ritter, K.; Kuschnierz, J.; Bormann, K.; Kaps, C.; Carvalho, C.; Mülhaupt, R.; Sittinger, M.; Gellrich, N. Bone repair by cell-seeded 3D-bioplotted composite scaffolds made of collagen treated tricalciumphosphate or tricalciumphosphate-chitosan- collagen hydrogel or PLGA in ovine critical-sized calvarial defects. *J. Biomed. Mater. Res., Part B* **2010**, *93*, 520.

(28) Neufurth, M.; Wang, X.; Schröder, H. C.; Feng, Q.; Diehl-Seifert, B.; Ziebart, T.; Steffen, R.; Wang, S.; Müller, W. E. G. Engineering a morphogenetically active hydrogel for bioprinting of bioartificial tissue derived from human osteoblast-like SaOS-2 cells. *Biomaterials* **2014**, *35*, 8810.

(29) Paxton, N.; Smolan, W.; Böck, T.; Melchels, F.; Groll, J.; Jungst, T. Proposal to assess printability of bioinks for extrusion-based

bioprinting and evaluation of rheological properties governing bioprintability. *Biofabrication* **2017**, *9*, No. 044107.

(30) Hermanson, G. T. *Bioconjugate Techniques*, 3rd ed., Audet, J.; Preap, M., Eds.; Elsevier Inc.: London, 2013.

(31) Rickett, T. A.; Amoozgar, Z.; Tuchek, C. A.; Park, J.; Yeo, Y.; Shi, R. Rapidly Photo-Cross-Linkable Chitosan Hydrogel for Peripheral Neurosurgeries. *Biomacromolecules* **2011**, *12*, 57.

(32) Ouyang, L.; Yao, R.; Zhao, Y.; Sun, W. Effect of bioink properties on printability and cell viability for 3D bioplotting of embryonic stem cells. *Biofabrication* **2016**, *8*, No. 035020.

(33) Ozbolat, I. T.; Hospodiuk, M. Current advances and future perspectives in extrusion-based bioprinting. *Biomaterials* **2016**, *76*, 321.

(34) Pereira, R. F.; Bártolo, P. J. 3D Photo-Fabrication for Tissue Engineering and Drug Delivery. *Engineering* **2015**, *1*, No. 090-112.

(35) Joas, S.; Tovar, G. E. M.; Celik, O.; Bonten, C.; Southan, A. Extrusion-Based 3D Printing of Poly(ethylene glycol) Diacrylate Hydrogels Containing Positively and Negatively Charged Groups. *Gels* **2018**, *4*, No. 69.

(36) Berger, J.; Reist, M.; Mayer, J. M.; Felt, O.; Peppas, N. A.; Gurny, R. Structure and interactions in covalently and ionically crosslinked chitosan hydrogels for biomedical applications. *Eur. J. Pharm. Biopharm.* **2004**, *57*, 19.

(37) Ang, T. H.; Sultana, F. S. a.; Hutmacher, D. W.; Wong, Y. S.; Fuh, J. Y. H.; Mo, X. M.; Loh, H. T.; Burdet, E.; Teoh, S. H. Fabrication of 3D chitosan-hydroxyapatite scaffolds using a robotic dispensing system. *Mater. Sci. Eng. C* **2002**, *20*, 35.

(38) Bergonzi, C.; Natale, A.; Di; Zimetti, F.; Marchi, C.; Bianchera, A.; Bernini, F.; Silvestri, M.; Bettini, R.; Elviri, L. Study of 3D-printed chitosan scaffold features after different post-printing gelation processes. *Sci. Rep.* **2019**, *9*, No. 362.

(39) Al-Ahmad, A.; Wiedmann-Al-Ahmad, M.; Carvalho, C.; Lang, M.; Follo, M.; Braun, G.; Wittmer, A.; Mülhaupt, R.; Hellwig, E. Bacterial and Candida albicans adhesion on rapid prototyping-produced 3D-scaffolds manufactured as bone replacement materials. *J. Biomed. Mater. Res. Part A* **2008**, *87A*, 933.

(40) Walker, J. M.; Lee, M.; Wu, B. Recent Advances in 3D Printing of Tissue Engineering Scaffolds. In *Computer-Aided Tissue Engineering SE-15*, Liebschner, M. A. K., Ed.; Humana Press, 2012; Vol. *868*, pp 257−267.

(41) Stauffer, S. R.; Peppast, N. A. Poly(vinyl alcohol) hydrogels prepared by freezing-thawing cyclic processing. *Polymer* **1992**, *33*, 3932.

(42) Annabi, N.; Nichol, J. W.; Zhong, X.; Ji, C.; Koshy, S.; Khademhosseini, A.; Dehghani, F. Controlling the Porosity and Microarchitecture of Hydrogels for Tissue Engineering. *Tissue Eng. Part B: Rev.* **2010**, *16*, 371.

(43) Lanasa, S. M.; Hoffecker, I. T.; Bryant, S. J. Presence of pores and hydrogel composition influence tensile properties of scaffolds fabricated from well-defined sphere templates. *J. Biomed. Mater. Res. Part B Appl. Biomater.* **2011**, *96B*, 294.

(44) Richtering, W.; Saunders, B. R. Gel architectures and their complexity. *Soft Matter* **2014**, *10*, 3695.

(45) Schipani, R.; Nolan, D. R.; Lally, C.; Kelly, D. J. Integrating finite element modelling and 3D printing to engineer biomimetic polymeric scaffolds for tissue engineering. *Connect. Tissue Res.* **2020**, *61*, 174.

(46) Zhu, J. Bioactive Modification of Poly(ethylene glycol) Hydrogels for Tissue Engineering. *Biomaterials* **2010**, *31*, 4639.

(47) Ahmadi, F.; Oveisi, Z.; Samani, S. M.; Amoozgar, Z. Chitosan based hydrogels: characteristics and pharmaceutical applications. *Res. Pharm. Sci.* **2015**, *10*, 1.

(48) Hadjipanayi, E.; Mudera, V.; Brown, R. A. Guiding cell migration in 3D: a collagen matrix with graded directional stiffness. *Cell Motil. Cytoskeleton* **2009**, *66*, 121.

(49) Vedadghavami, A.; Minooei, F.; Mohammadi, M. H.; Khetani, S.; Rezaei Kolahchi, A.; Mashayekhan, S.; Sanati-Nezhad, A. Manufacturing of hydrogel biomaterials with controlled mechanical properties for tissue engineering applications. *Acta Biomater.* **2017**, *62*, 42.

(50) Darby, I. A.; Laverdet, B.; Frederic, B.; Desmouliere, A. Fibroblasts and myofibroblasts in wound healing. *Clin. Cosmet. Investig. Dermatol.* **2014**, *7*, 301.

(51) Li, X.-J.; Huang, F.-Z.; Wan, Y.; Li, Y.-S.; Zhang, W. K.; Xi, Y.; Tian, G.-H.; Tang, H.-B. Lipopolysaccharide Stimulated the Migration of NIH3T3 Cells Through a Positive Feedback Between β-Catenin and COX-2. *Front. Pharmacol.* **2018**, *9*, 1487.

(52) Bektas, N.; Şenel, B.; Yenilmez, E.; Özatik, O.; Arslan, R. Evaluation of wound healing effect of chitosan-ased gel formulation containing vitexin. *Saudi Pharm. J.* **2020**, *28*, No. 87.

(53) Conley, G. M.; Zhang, C.; Aebischer, P.; Harden, J. L.; Scheffold, F. Relationship between rheology and structure of interpenetrating, deforming and compressing microgels. *Nat. Commun.* **2019**, *10*, No. 2436.

(54) Rheology: An Introduction - TA Instruments. Texas A & M Rheology Workshop, https://www.tainstruments.com/wp-content/uploads/2019-04-AM-Rheology.pdf (accessed April 19, 2019).